China Ocean Eng., Vol. 27, No. 5, pp. 671 – 682

DOI 10.1007/s13344-013-0056-2, ISSN 0890-5487

Developing Serpent-Type Wave Generators to Create Solitary Wave Simulations with BEM*

Wen-Kai WENG[a], Ruey-Syan SHIH[b, 1] and Chung-Ren CHOU[a]

[a] *Department of Harbour & River Engineering, National Taiwan Ocean University, Keelung 20224, China*

[b] *Department of Construction and Spatial Design, Tungnan University, New Taipei 22202, China*

(Received 19 January 2011; received revised form 16 May 2013; accepted 28 June 2013)

ABSTRACT

Developing serpent-type wave generators to generate solitary waves in a 3D-basin was investigated in this study. Based on the Lagrangian description with time-marching procedures and finite differences of the time derivative, a 3D multiple directional wave basin with multidirectional piston wave generators was developed to simulate ocean waves by using BEM with quadrilateral elements, and to simulate wave-caused problems with fully nonlinear water surface conditions. The simulations of perpendicular solitary waves were conducted in the first instance to verify this scheme. Furthermore, the comparison of the waveform variations confirms that the estimation of 3D solitary waves is a feasible scheme.

Key words: *boundary element method*; *quadrilateral element*; *3D wave basin*; *time domain*; *solitary wave*; *nonlinear wave*

1. Introduction

Numerical wave basin is used to evaluate wave impact on coastal structures. The variations of oceanic physical characteristics must be accurately predicted to reproduce certain aspects of near-shore wave activity. Numerous investigations on 3D numerical models regarding the simulation of nonlinear waves have been enthusiastically established which thanks to the rapid development of personal computers in the last two decades. The development of a 3D numerical wave basin in practical applications that use personal computers has been an arduous task due to the considerable quantities of arithmetic units; therefore, simulations of fully nonlinear waves in 3D models were in straitened circumstances. Until recently, these difficulties have been overcome by innovation and great advancements in computer science. These innovations and advancements shortened the arithmetic time of modeling. To overcome the problem previously mentioned, parallel computing techniques on PC clusters were adopted in the present study for calculations and will be discussed in a later section.

By using a number of wavemakers as an absorption facility, a method for active absorption of multidirectional waves in a 3D numerical wave tank model (NWT) was presented by Skourup and Schäffer (1998) based on a traditional 2D active absorption method, i.e. 2D-AWACS (Active Wave

* The work was financially supported by the Science Council under the Project Nos. NSC-95-2221-E-019-075-MY3 (CRC) and NSC-97-2221-E-236-011-(RSS).

1 Corresponding author. Email: rsshih@mail.tnu.edu.tw

Absorption Control System). Uni- as well as multi-directional wave can be generated by a serpent type wave generator according to linear wave maker theory (Dean and Darlymple, 1993) for each segment. Practical application of this theory includes generators such as "snake-type", "serpent-type", or "segmented" wave generator in a physical laboratory. Unidirectional and multi-directional waves can be generated spatially by sinusoidal motion and from the basic "snake principle" of the segments of a serpent-type wave generator, respectively. The incident waves were generated by prescribing motions as a series of piston wave makers.

The directional wave maker theory with sidewall reflections developed by Dalrymple was experimentally confirmed by Mansard and Miles (1994). Similar experimental investigations on the applicability and reproducibility of the multi-face generators with small segments were made by Hiraishi *et al.* (1995). An optimization method to improve the uniformity of monochromatic oblique waves in a wave basin was adopted by Matsumoto and Hanzawa (1996) using the non-linear least square formulation to determine individual paddle motions of a multi-directional wave maker. Shih *et al.* (2009) made the improvements on the oblique planar wave train in a basin generated by multiple irregular wave generators and numerically investigated those improvements adopting the boundary element method (BEM). Simulations of perpendicular waves were conducted in the first instance to verify the scheme, and proceeded with the generations and propagations of oblique waves in a large angle. Li *et al.* (2011) developed a simulation method to generate waves by two-sided segmented wave-makers. This paper introduces the two-sided segmented wave-makers and the wave simulation methods on long-crested waves, short-crested waves, and irregular waves. However, development of 3D NWT remains rather difficult, because an extremely long CUP time (tremendous computing time) and extensive memory capacity are required for a fully nonlinear numerical model by means of 3D BEM to solve fully nonlinear problems directly in time domain, and the influence matrix needs to be set up and inverted at each time step as the nodes on the free surface move to new positions.

This study investigated the application of 3D BEM to the serpent-type wave generator for solitary wave generations. The generations of a perpendicular moving solitary wave were presented through prescribing adequate snakelike motions at the input boundary of the wave maker. As an alternative to physical wave basin, a 3D algorithm based on BEM with linear tetragonal elements was developed to model the generation of a solitary wave, and boundary values were updated at each time step by a forward difference time marching procedure.

2. Numerical Modeling and Simulations

2.1 Theoretical Development and Boundary Conditions

The 3D numerical wave basin with constant water depth h contains a segmented wave generator that occupies one wall of the wave basin (Fig. 1). The Cartesian coordinates (x, y, z) were employed, the region of which was bounded by the free water surface, Γ_1, the segmented wave generator, Γ_2, the right and left lateral impermeable sidewalls, Γ_3 and Γ_4, the impermeable across wall from the generators, Γ_5, and an impermeable bottom, Γ_6. Under the assumption of an inviscid, incompressible, and homogeneous (irrotational) fluid within the region $\Omega(t)$, the solution of velocity potential $\Phi(x, y, z; t)$

is given to satisfy the following Laplace equation:

$$\frac{\partial^2 \Phi}{\partial x^2}+\frac{\partial^2 \Phi}{\partial y^2}+\frac{\partial^2 \Phi}{\partial z^2}=0. \tag{1}$$

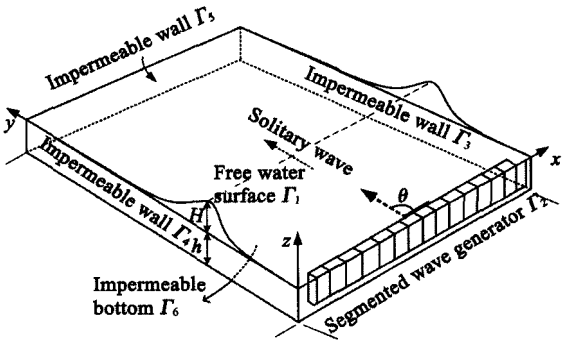

Fig. 1. Definition sketch of 3D-wave basin with segmented wave generator.

Based on the Lagrangian description and time-marching procedure with finite differencing of the time derivative, the undisturbed free surface, the fully nonlinear kinematic and dynamic boundary conditions can be obtained (see Shih *et al.*, 2009).

The boundaries of the three vertical walls, referred to as Γ_3, Γ_4, and Γ_5, and the stationary bottom, Γ_6, are impermeable, and the no-flow boundary conditions are prescribed as:

$$\frac{\partial \Phi}{\partial n}=0, \quad \text{on} \quad \Gamma_3,\ \Gamma_4,\ \Gamma_5, \text{ and } \Gamma_6, \tag{2}$$

where n is the unit outward normal vector. In accordance with the continuity of the velocities of the wave paddle and that of adherent water particles, the velocities are extrapolated at the interface without the distinction between the wave paddle and fluid. The boundary condition on the wave-paddles is obtained through:

$$\frac{\partial \Phi_k}{\partial n}=-U(x;t), \quad \text{on} \quad \Gamma_2, \tag{3}$$

where k represents the series number of wave paddles.

The boundary condition in Eq. (3) for the generation of a solitary wave can be derived from the Boussinesq equation expressed as:

$$U(x,t)=H\sqrt{\frac{g}{h}}\cdot \sec h^2\left[\sqrt{\frac{3\zeta_0}{4h^3}}C(t-t_c)-x\cos\theta\right]; \tag{4}$$

$$C=\sqrt{g(h+H)}, \tag{5}$$

where H is the wave height; g, C, h, and θ are the gravitational acceleration, wave celerity, still water depth, and the angle of incident wave, respectively; t_c is a characteristics time scale, which is defined as half the time of the stroke.

2.2 Algorithm and Differencing Scheme

The boundary value problem for the velocity potential was solved by the boundary integral equation based on Green's second identity; the velocity potential within the region was solved by using

the velocity potential $\Phi(\xi_x,\xi_y,\xi_z;t)$ and its normal derivative $\partial\Phi(\xi_x,\xi_y,\xi_z;t)/\partial n$ on the boundaries. The corresponding 3D free space Green's function is defined as:

$$\alpha\Phi(x,y,z;t)=\int_\Gamma\left\{\frac{\partial\Phi(\xi_x,\xi_y,\xi_z;t)}{\partial n}G(\varsigma,\chi)-\Phi(\xi_x,\xi_y,\xi_z;t)\frac{\partial G(\varsigma,\chi)}{\partial n}\right\}\mathrm{d}\Gamma \tag{6}$$

$$\alpha(\chi)=\begin{cases}1 & \text{inside the fluid domain}\\ 1/2 & \text{on the smooth boundary}\\ 0 & \text{outside the fluid domain}\end{cases}$$

where

$$G(\varsigma,\chi)=\frac{1}{4\pi r} \tag{7}$$

with

$$\frac{\partial G(\varsigma,\chi)}{\partial n}=\bar{G}(\varsigma,\chi)=\frac{-1}{4\pi r^2}\frac{\partial r}{\partial n}; \tag{8}$$

$$\chi=(x,y,z); \tag{9}$$

$$\varsigma=(\xi_x,\xi_y,\xi_z); \tag{10}$$

$$r=|\varsigma-\chi|=\sqrt{(\xi_x-x)^2+(\xi_y-y)^2+(\xi_z-z)^2}\,. \tag{11}$$

Linear quadrilateral element was adopted in this study, which was defined by its four corner points, and the location of each node within the element would take a process of the conformal mapping from the Cartesian coordinates (x, y, z) to the local coordinates (ξ_1,ξ_2,η), as shown in Fig. 2. ξ_1, ξ_2, and η are the three directions corresponding to local coordinates x, y, and z. Thus, the velocity potential and its normal derivative at the node can be written as:

$$\Phi(\xi_x,\xi_y,\xi_z,t)=\sum_{k=1}^{4}\Psi_k\Phi_k(\xi_x,\xi_y,\xi_z,t), \tag{12}$$

where

$$\Psi_1=\frac{1}{4}(1-\xi_1)(1-\xi_2),\ \ \Psi_2=\frac{1}{4}(1+\xi_1)(1-\xi_2),$$
$$\Psi_3=\frac{1}{4}(1+\xi_1)(1+\xi_2),\ \ \Psi_4=\frac{1}{4}(1-\xi_1)(1+\xi_2). \tag{13}$$

2.3 Integral Formulation and Discretization

The domain of a 3D model was bounded by six different boundaries; therefore, Eq. (6) can be rearranged and written as:

$$\alpha\Phi(x,y,z,t)+\sum_{p=1}^{6}\int_{\Gamma_p}\Phi(\xi_x,\xi_y,\xi_z,t)\bar{q}\mathrm{d}A=\sum_{p=1}^{6}\int_{\Gamma_p}\bar{\Phi}(\xi_x,\xi_y,\xi_z,t)q\mathrm{d}A\,. \tag{14}$$

The integral representation of the solution for the Green function may be written for the discretized boundaries, N_p (p=1–6), and linear quadrilateral element as:

$$\alpha\Phi_i(x,y,z,t)+\sum_{p=1}^{6}\sum_{j=1}^{N_p}\sum_{s=1}^{4}h_{ij}^{s}\Phi_j(\xi_x,\xi_y,\xi_z,t)=\sum_{p=1}^{6}\sum_{j=1}^{N_p}\sum_{s=1}^{4}g_{ij}^{s}\overline{\Phi}_j(\xi_x,\xi_y,\xi_z,t) \tag{15}$$

where

$$h_{ij}^{s}=-\frac{1}{8\pi}\int_{-1}^{1}\int_{-1}^{1}\Psi_s\frac{1}{r^2}\frac{\partial r}{\partial n}|G|_{\Gamma_{ij}}\,\mathrm{d}\xi\mathrm{d}\eta \qquad (s=1\text{–}4); \tag{16}$$

$$g_{ij}^{s}=\frac{1}{8\pi}\int_{-1}^{1}\int_{-1}^{1}\Psi_s\frac{1}{r}|G|_{\Gamma_{ij}}\,\mathrm{d}\xi\mathrm{d}\eta \qquad (s=1\text{–}4). \tag{17}$$

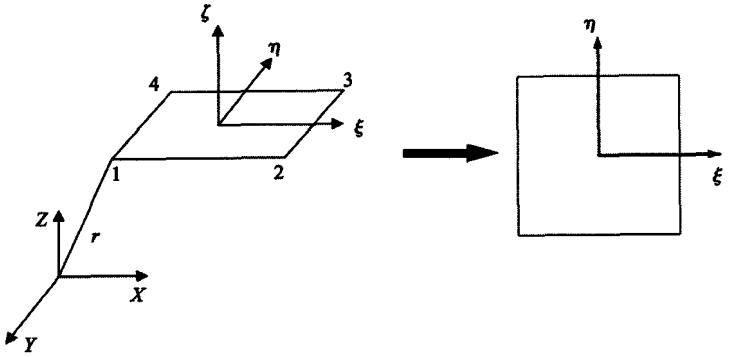

Fig. 2. Definition sketch of conformal mapping process from triangular unit to dimensionless quadrate element.

The above equations can be written in a dissolution form and are contingent on domain integral from utilizing a Gauss integration to proceed with the calculations. And the equations will be discussed under two circumstances, i.e. when $i\neq j$ and $i=j$:

when $i\neq j$:

$$h_{ij}^{s}=-\frac{1}{8\pi}\sum_{l=1}^{n}\sum_{m=1}^{n}w_l w_m\Psi_s\frac{1}{r_{ilm}^2}\frac{\partial r_{ilm}}{\partial n}|G|_{\Gamma_{ij}} \qquad (s=1\text{–}4); \tag{18}$$

$$g_{ij}^{s}=\frac{1}{8\pi}\sum_{l=1}^{n}\sum_{m=1}^{n}w_l w_m\Psi_s\frac{1}{r_{ilm}}|G|_{\Gamma_{ij}} \qquad (s=1\text{–}4), \tag{19}$$

where

$$|G|_{\Gamma_{ks}}=\sqrt{g_1^{\,2}+g_2^{\,2}+g_3^{\,2}} \qquad (s=1\text{–}4); \tag{20}$$

$$g_1=\frac{\partial y}{\partial\xi}\frac{\partial z}{\partial\eta}-\frac{\partial z}{\partial\xi}\frac{\partial y}{\partial\eta},\ g_2=\frac{\partial z}{\partial\xi}\frac{\partial x}{\partial\eta}-\frac{\partial x}{\partial\xi}\frac{\partial z}{\partial\eta},\ g_3=\frac{\partial x}{\partial\xi}\frac{\partial y}{\partial\eta}-\frac{\partial y}{\partial\xi}\frac{\partial x}{\partial\eta}; \tag{21}$$

$$\frac{\partial r_{ilm}}{\partial n}=\frac{x_{lm}-x_i}{r_{ilm}}\left(\frac{\partial x}{\partial n}\right)_j+\frac{y_{lm}-y_i}{r_{ilm}}\left(\frac{\partial y}{\partial n}\right)_j+\frac{z_{lm}-z_i}{r_{ilm}}\left(\frac{\partial z}{\partial n}\right)_j, \tag{22}$$

where r_{ilm} represents the distance between the source i and the evaluated point over integrated segment j using Gaussian integration, and w_l and w_m are the weighting functions.

when $i=j$:

As a result of $\partial r/\partial v=0$, we acquire:

$$h_{ij}^{s}=0 \qquad (s=1\text{–}4). \tag{23}$$

The integrals of Eqs. (18) and (19) exist as singularities as i approaches j, in which r corresponds to r_i, i.e. r_{ilm} approaches to zero. The singularities occur when the base point and field point coincide and are not integrable; thus, the regular Gaussian does not give accurate results under this circumstance. We, therefore, should remedy the situation by rearranging the polynomial approximation for g_{ij}^s as follows.

An eigenvalue can be found in Eq. (22) when $i=j$, which was processed by the following treatment (Fig. 3), and the four nodes of each quadrilateral element being marked as P_1, P_2, P_3 and P_4, were first segmented into two triangular elements and expressed as $\Delta P_1P_2P_3$ and $\Delta P_1P_3P_4$. When the occurrence of $i=j$ happened on P_1 , each node within the unit was to be transformed to homogeneous coordinate by conformal mapping process. The triangular units eventually concluded with the mapping of the above triangular unit to dimensionless quadrate element.

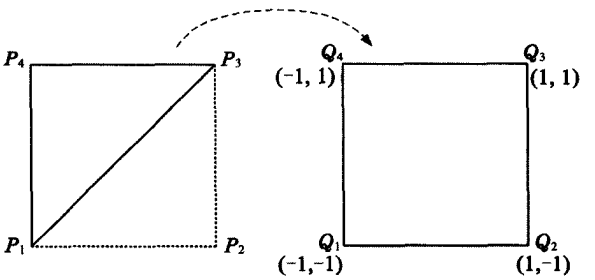

Fig. 3. Unit transformed to homogeneous coordinate by conformal mapping process.

The boundary value problem for the velocity potential is solved by the boundary:

$$g_{ij}^{1}=\frac{1}{8\pi}\sum_{l=1}^{n}\sum_{m=1}^{n}w_l w_m\left(1-\xi_l-\eta_m+\xi_l\eta_m\right)\frac{1}{r_{ilm}^{*}}\left|G^{*}\right|_{\Gamma_{k1}}; \tag{24}$$

$$g_{ij}^{2}=\frac{1}{8\pi}\sum_{l=1}^{n}\sum_{m=1}^{n}w_l w_m\left(1+\xi_l-\eta_m-\xi_l\eta_m\right)\frac{1}{r_{ilm}^{*}}\left|G^{*}\right|_{\Gamma_{k2}}; \tag{25}$$

$$g_{ij}^{3}=\frac{1}{8\pi}\sum_{l=1}^{n}\sum_{m=1}^{n}w_l w_m\left(1+\xi_l+\eta_m+\xi_l\eta_m\right)\frac{1}{r_{ilm}^{*}}\left|G^{*}\right|_{\Gamma_{k3}}; \tag{26}$$

$$g_{ij}^{4}=\frac{1}{8\pi}\sum_{l=1}^{n}\sum_{m=1}^{n}w_l w_m\left(1-\xi_l+\eta_m-\xi_l\eta_m\right)\frac{1}{r_{ilm}^{*}}\left|G^{*}\right|_{\Gamma_{k4}}, \tag{27}$$

where

$$\left|G^{*}\right|_{\Gamma_{ks}}=\sqrt{g_1^{*2}+g_2^{*2}+g_3^{*2}}\qquad (s=1\text{–}4); \tag{28}$$

$$g_1^{*}=\frac{\partial y^{*}}{\partial\xi}\frac{\partial z}{\partial\eta}-\frac{\partial z^{*}}{\partial\xi}\frac{\partial y}{\partial\eta},\ g_2^{*}=\frac{\partial z^{*}}{\partial\xi}\frac{\partial x}{\partial\eta}-\frac{\partial x^{*}}{\partial\xi}\frac{\partial z}{\partial\eta},\ g_3^{*}=\frac{\partial x^{*}}{\partial\xi}\frac{\partial y}{\partial\eta}-\frac{\partial y^{*}}{\partial\xi}\frac{\partial x}{\partial\eta}, \tag{29}$$

r_{ilm} represents the distance between the source i and the evaluated point (ξ_l,η_m) over the integrated segment j using Gaussian integration.

2.4 Boundary Conditions on Wave Paddles

The 3D numerical wave basin contains a series of segmented wave generators that occupy one wall of 40 segmented pseudo wavemakers. The oscillating motion of the arrayed wave makers in a physical wave basin may be a rather difficult job for the numerical model due to the discontinuous phase motion between each wave board. This can be solved by considering each node as a hinge that links the detached segments (Fig. 4). Waves are generated separately by a series of serpent-type wave generators, particularly the possibility of the continuity of the produced wave crest lines. For multi-directional wave generation, oblique waves can be generated by setting different phases between adjacent segments. A numerical serpentiform motion is also established by prescribing the velocities based on the fluid particles velocities of water wave theory with a series of piston-type wave generators.

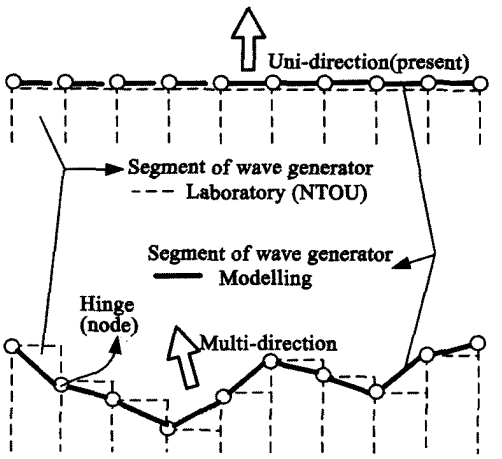

Fig. 4. Phase motion between each wave board with hinge that links the detached segmented wave boards.

The boundary condition for the generation of solitary wave can be derived from the Boussinesq equation expressed in Eqs. (4) and (5). For periodical wave generation, the boundary condition $U(t)$ on the series generators is given by:

$$U(x,t)=\zeta_0\alpha(f)\,\sigma\sin(\sigma t-kx\cos\theta)\,. \tag{30}$$

For short-crested wave generation, the boundary condition $U(t)$ is expressed as:

$$U(x,t)=\zeta_1\alpha(f_1)\,\sigma_1\sin(\sigma_1 t-x\cos\theta_1)+\zeta_2\,\alpha(f_2)\,\sigma_2\sin(\sigma_2 t-x\cos\theta_2) \tag{31}$$

and

$$\alpha(f)=\frac{\sinh(kh)\cosh(kh)+kh}{2\sinh^2(kh)}, \tag{32}$$

where σ, ζ_o, k, h, θ and $\alpha(f)$ denote the angular frequency, the incident wave height, the wave number, the water depth, the angle of incident wave, and the transfer function, respectively. In Eq. (31), the footnotes "1" and "2" denote the first and second conditions of the two intersecting waves. The generations of oblique regular waves and short-crested waves will be a rudimentary debate in the following discussion.

2.5 Parallel Computation on A PC Cluster

To simulate wave deformation more authentically, meshes were segmented more delicately on the water surface. The quantity of nodes on the free water surface requires 121×41 nodes, and further, the inclusion of the other five surfaces makes a total amount of 5914 nodes. As a result, an arrangement for the matrix of order 5914×5914 was required when calculating. We wrote the square matrix of order 5914. The influence matrix must be set up and solved for every time step since the computational domain continuously changes, and the computation requires substantial CPU time and iterative solvers. Therefore, the modeling of 3D NWT using a single personal computer (PC) is unfeasible, massive parallel computing systems and PC clusters are used. Effective parallel programming has become critical to the development of 3D numerical model. The PC cluster is established by parallel connections of numerous PCs, and in this study, eight PCs were used. The computation was carried out using message passing interface (MPI) parallel language and MPICH software developed by the American Argonne National Laboratory and Mississippi State University. MPICH is a free, high-performance, and widely portable implementation of MPI. A standard for message-passing between distributed-memory applications used in parallel computing was developed and authored by Mathematics and Computer Science Division (Argonne National Laboratory) and Department of Computer Science, University of Illinois at Urbana-Champaign. In computation, iterations were performed collaboratively by different PCs simultaneously. The data were transferred to the designated PC to complete the computation. Each PC cluster we use comprises eight interconnected dual Pentium 4 CPUs workstations, with which the parallel matrix factorization algorithm was developed to solve the resulting large matrix and the original inverse matrix was partitioned into eight submatrices for parallel computation.

3. Numerical Examples and Discussion

3.1 Generation of Oblique Waves

The generation, propagation, and deformation of a solitary wave in a 3D wave basin with a constant water depth h were simulated. The size of the basin is 40 m×20 m×0.5 m and 40 m×20 m×1.0 m, and the wave height was H=0.2 m and the time interval was $\Delta t = t_c / 100$. The boundaries, $\Gamma_1 \sim \Gamma_6$, were divided into $N_1 \sim N_6$ discrete elements, where N_1=1681, N_2=42, N_3=82, N_4=82, N_5=82 and N_6=441. Although the wave field was produced based on the snake principle, the spatially sinusoidal motion of a serpent-type wave maker would produce any desired type of waves propagating obliquely to the plane. However, the finite width of the basin with fully reflecting sidewalls resulted in the wave generations influenced by sidewall reflections. The unidirectional solitary wave propagation was first carried out for simplicity, and to verify the validity of the numerical scheme.

The variation of the wave height for oblique wave was verified by the generation of periodical regular waves. Fig. 5 shows the spatial distributions of velocity in x-y plane to the generations of oblique regular wave in different time steps using Eq. (30). In a multi-directional 3D wave basin composed of multi-face serpent-type wave generators with individual controlled paddles, the motion of

each piston is governed by a control signal that is calculated directly by Eqs. (3)–(5). Fig. 6 shows the case for a short crested wave propagating with an inclined angle θ of 70° by Eq. (31). Owing to the influences of both sides of the perpendicular walls, the simulation process lasts only four to five periods of generations, and Fig. 6a shows the profile and Fig. 6b shows the wave heights distribution of oblique short-crested wave propagating in direction of θ=70° with $\sigma^2 h/g$=0.5 and $\Delta t=t_c/100$. Accordingly, this study simply discusses the generation and the application of perpendicularly propagating long-wave (solitary wave) to support the research on and the application of the oblique wave generation and two-sided segmented wave-makers (L-shaped) or U-shaped wave tanks.

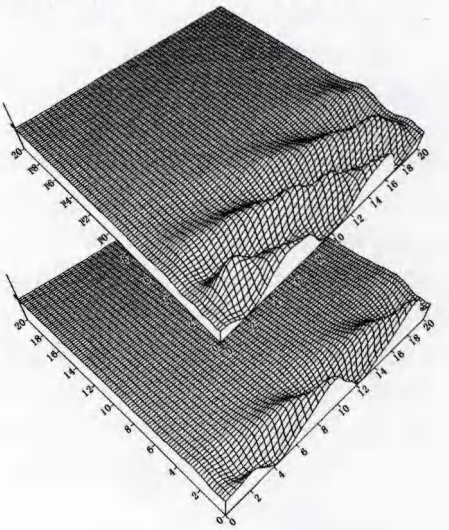

Fig. 5. Generation of oblique wave propagating in the direction of θ=70° with $\sigma^2 h/g$=0.5 and $\Delta t=t_c/100$.

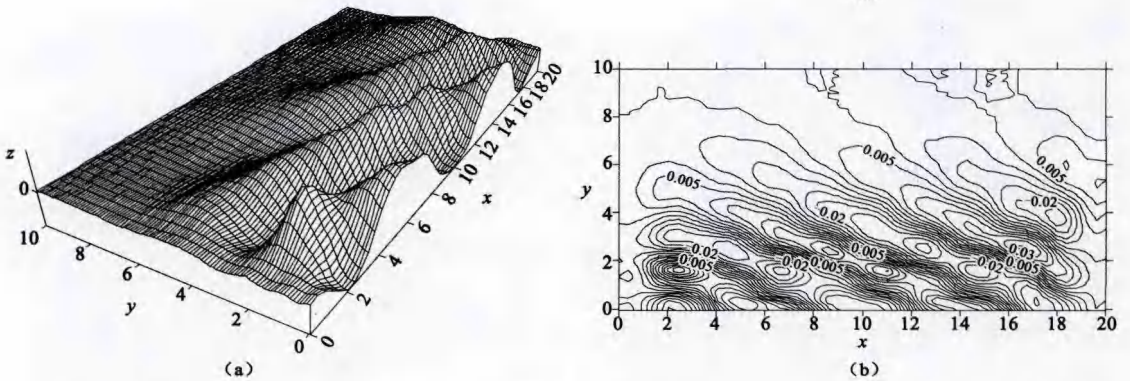

Fig. 6. Wave profile (a) and wave height distribution (b) of oblique short-crested wave propagating in direction of θ=70° with $\sigma^2 h/g$=0.5 and $\Delta t=t_c/100$.

3.2 Discussions on the Generation of Solitary Waves

The generation and propagation of a solitary wave in a constant wave basin are demonstrated with h=0.5 m. A solitary wave accompanied by a co-propagating wave in its tail is detected. The previous research has discussed the reduction of trailing waves, which are presented in solitary waves, specifically in experimental investigations where the solitary wave is generated in a lab. Even though the

conditions on the paddle are exactly the same in some cases, it is found that the amplitude of the co-propagating oscillatory tail trailing behind the wave depends on the amplitude of the solitary wave.

Various investigations point out that the classical solitary wave solutions will rapidly decay to naught in its tail regions. Because of this instability, we replace the classical solitary wave with a generalized solitary wave containing a co-propagating oscillatory tail. A small trailing oscillatory wave train behind the rear wave was found by Bona *et al.* (1980) in their solutions of Peregrine's nonlinear long wave equation. As illustrated by Fenton and Rienecker (1982), this oscillatory tail appears only when the initial wave heights are larger than 0.3 m and could not be obtained from solutions of the KdV equation, which is a model for the propagation of unidirectional long waves of small amplitude, i.e., soliton. A wave train trailing behind each of the emerging solitary waves was also found in the numerical investigation of the collision between two solitary waves by Mirie and Su (1982). And many attempts and studies are being carried out for the minimization of trailing waves.

The minimization of the trailing waves between numerical and experimental results was compared and discussed by Sriram (2007), whose study shows that the trailing wave is reduced by modifying the input signal with different upward and downward accelerations. Sriram (2007) suggested that this could also be done by increasing the stroke and adjusting the upward and downward acceleration.

It is mentioned that the trailing wave trains are related to the amplitude of the solitary wave; thus, the higher wave steepness—respectively in Fig. 7 and Fig. 8—is set. In the cases of H/h=0.15 and 0.20, the trailing waves are obviously found but the solitary wave to propagate the opposite. Nevertheless, the modeling is successful, precise and on a step-by-step basis.

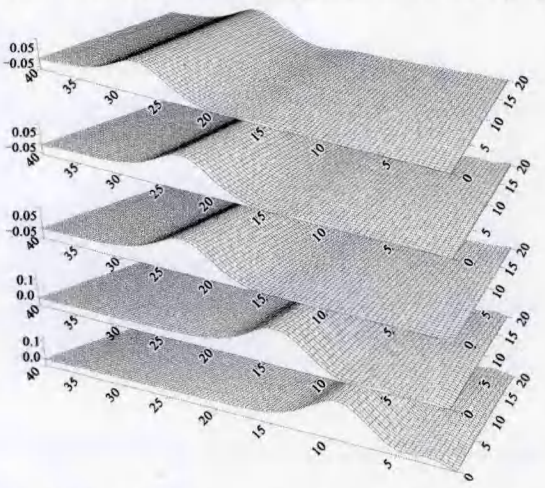

Fig. 7. Generation and propagation of solitary with H/h=0.15 and $\Delta t=t_c/20$.

Fig. 8. Generation and propagation of solitary with H/h=0.20 and $\Delta t=t_c/20$.

3.3 Conservation of Mass and Energy

The present numerical model was validated through convergence test according to the conservation of mass and energy. The total energy within the basin has to remain invariable when the pseudo wave board stops moving after the solitary wave is generated. Therefore, if a dispersive tail is produced, the

amplitude of the solitary wave should be slightly decreased as a result of the fractional energy transfer to the dispersive tail.

The conservative property can be crosschecked through the following formulae:

$$M = \int_{\Gamma(t)} \zeta (e_z \cdot n) \mathrm{d}\Gamma ; \tag{33}$$

$$E_\mathrm{p}(t) = \frac{1}{2} g \int_{\Gamma(t)} \zeta^2 (e_z \cdot n) \mathrm{d}\Gamma ; \tag{34}$$

$$E_\mathrm{k}(t) = \frac{1}{2} \int_{\Gamma(t)} \Phi \cdot \bar{\Phi} \mathrm{d}\Gamma ; \tag{35}$$

$$E(t) = E_\mathrm{k}(t) + E_\mathrm{p}(t) , \tag{36}$$

where M, E, E_k, and E_p denote the total mass of the waveform, the total energy, the kinetic and potential energy, respectively.

Fig. 9 shows the total energy E is approximately equal to 2.73 and remains unchanged when the time interval $\Delta t = t_c/100$. The same phenomenon is also found for the kinetic energy E_k and potential energy E_p, but E, E_k, and E_p slightly increase or decrease after t=2.3 s. Furthermore, the total mass, M rises to 8.8 m^3 after the solitary wave is formed; nevertheless, the total mass decreases along with the propagation of the wave. This may be due to dimensions of time interval and the repetition of the calculation, because the model was established with a time marching procedure. Therefore, the attenuation of mass may be the cause of numerical errors. Although a parallel computing system was utilized, it still took a long time for the calculation to complete. Since the meshes on the water surface were more delicately segmented, the segmentation of time spacing Δt with element size Δs was likely to cause large instability and errors of the scheme. Thus, the calculation process of convergence and stability still needs to be improved for better results in the conservation of mass and energy.

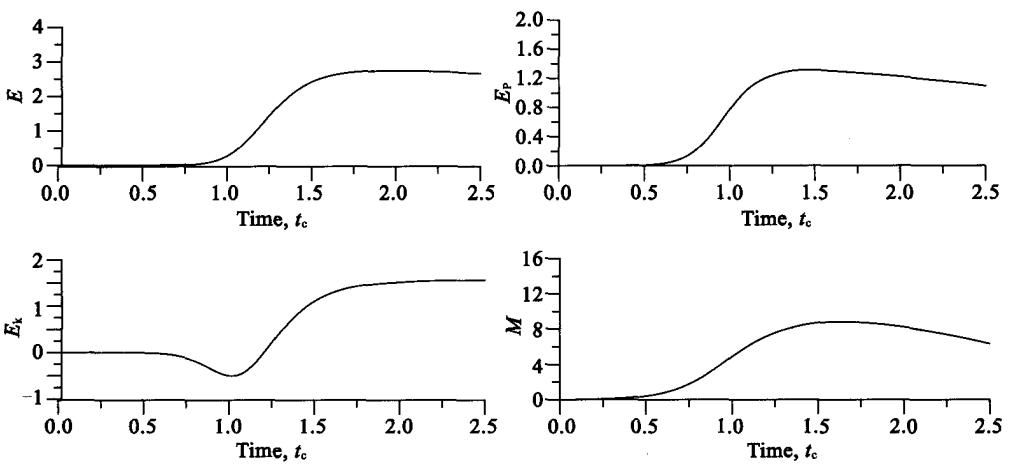

Fig. 9. Total mass, energy, potential energy and kinetic energy with H/h=0.05, h=1 m, and $\Delta t = t_c/100$.

4. Conclusion

The numerical simulation of 3D wave making problem of serpent-type wave generators to

generate solitary waves with fully nonlinear water surface condition in the basin are presented. The unidirectional solitary wave propagation was first carried out to verify the validity of the numerical scheme. This study provided proof to the validity of Boussinesq equations for the generation of a 3D solitary wave. A solitary wave accompanied by a co-propagating wave in its tail was detected. This study also shows: the amplitude of the co-propagating oscillatory tail trailing behind the wave is related to the amplitude of the solitary wave; the oscillation of the preceding trailing wave was on a conspicuous increase along with the enlargement of H/h; numerical errors-caused side effects can be reduced by the retrenchment of the time interval; a reduction of time step interval could improve the accuracy and stability. The method developed in this paper can be extended to oblique wave generation.

References

Bona, J. L., Pritchard, W. G. and Scott, L. R., 1980. Solitary-wave interaction, *Phys. Fluids*, **23**(3): 438–441.

Dean, R. G. and Darlymple, R. A., 1993. *Water Wave Mechanics for Engineers and Scientists*, Prentice Hall, Inc.

Fenton, J. D. and Rienecker, M. M., 1982. A Fourier method for solving nonlinear water-wave problems: Application to solitary-wave interactions, *J. Fluid Mech.*, **118**, 411–443.

Hirashi, T., Kanazawa, T. and Fujisaku, H., 1995. Development of multi-face directional random wave maker, *Proc. 5th Int. Offshore Polar Eng. Conf.*, Hague, Netherlands, **3**, 26–33.

Li, J., Chen, G., Yang, J. M. and Peng, T., 2011. Simulation method of wave generated by two-sided segmented wavemakers in deep ocean basin, *The Ocean Eng.*, **29**(3): 37–42. (in Chinese)

Mansard, E. P. D. and Miles, M. D., 1994. Experimental validation of directional wave maker theory with side wall reflections, *Int. J. Offshore Polar Eng.*, **4**(4): 273–277.

Matsumoto, A. and Hanzawa, M., 1996. New optimization method for paddle motion of multi-directional wavemaker, *Proc. 25th Conf. Coast. Eng.*, Orlando, FL. USA, **1**, 479–492.

Mirie, R. M. and Su, C. H., 1982. Collisions between solitary waves, Part 2. A numerical study, *J. Fluid Mech.*, **115**, 475–492.

Shih, R. S., Chou, C. R. and Weng, W. K., 2009. Numerical modelling of 3D oblique waves by L-type multiple directional wave generator, *Proc. 19th Int. Offshore Polar Eng Conf*, Osaka, Japan, **3**, 918–925.

Skourup, J. and Schäffer, H. A., 1998. Simulations with a 3D active absorption method in a numerical wave tank, *Proc. 8th Int. Offshore Polar Eng Conf*, Montréal, Canada, **3**, 107–115.

Sriram, V., 2007. *Solitary Waves and PIV Measurements*, IGAW Report, University of Wuppertal, Germany.